

# Nanoscale doping of polymeric semiconductors with confined electrochemical ion implantation

Received: 4 May 2023

Accepted: 18 March 2024

Published online: 22 April 2024

 Check for updates

Lanyi Xiang<sup>1,2</sup>, Zihan He<sup>1,2</sup>, Chaoyi Yan<sup>2</sup>, Yao Zhao<sup>1</sup>, Zhiyi Li<sup>1</sup>, Lingxuan Jia<sup>1,2</sup>, Ziling Jiang<sup>2</sup>, Xiaojuan Dai<sup>1</sup>, Vincent Lemaire<sup>3</sup>, Yingqiao Ma<sup>1</sup>, Liyao Liu<sup>1</sup>, Qing Meng<sup>1</sup>, Ye Zou<sup>1</sup>, David Beljonne<sup>3</sup>, Fengjiao Zhang<sup>2</sup>✉, Deqing Zhang<sup>1</sup>, Chong-an Di<sup>1</sup>✉ & Daoben Zhu<sup>1</sup>

Nanoresolved doping of polymeric semiconductors can overcome scaling limitations to create highly integrated flexible electronics, but remains a fundamental challenge due to isotropic diffusion of the dopants. Here we report a general methodology for achieving nanoscale ion-implantation-like electrochemical doping of polymeric semiconductors. This approach involves confining counterion electromigration within a glassy electrolyte composed of room-temperature ionic liquids and high-glass-transition-temperature insulating polymers. By precisely adjusting the electrolyte glass transition temperature ( $T_g$ ) and the operating temperature ( $T$ ), we create a highly localized electric field distribution and achieve anisotropic ion migration that is nearly vertical to the nanotip electrodes. The confined doping produces an excellent resolution of 56 nm with a lateral-extended doping length down to as little as 9.3 nm. We reveal a universal exponential dependence of the doping resolution on the temperature difference ( $T_g - T$ ) that can be used to depict the doping resolution for almost infinite polymeric semiconductors. Moreover, we demonstrate its implications in a range of polymer electronic devices, including a 200% performance-enhanced organic transistor and a lateral p–n diode with seamless junction widths of <100 nm. Combined with a further demonstration in the scalability of the nanoscale doping, this concept may open up new opportunities for polymer-based nanoelectronics.

Nanoresolved doping lays the foundation for modern semiconductor electronics. For polymeric semiconductors, nanoscale doping is crucial to unlock the full potential of their versatile molecular electronic states, and mechanically soft properties are required for highly integrated flexible and stretchable electronics<sup>1–3</sup>. State-of-the-art

silicon-based electronics primarily rely on ion-implantation processes involving nanostencils, for example, high-resolution lithography or pierced atomic force microscope (AFM) tips, to achieve nano- and even atomic-scale doping<sup>4,5</sup>. These routes have, however, proven unsuccessful for polymers because the weakly interacting conjugated

<sup>1</sup>Beijing National Laboratory for Molecular Sciences, CAS Key Laboratory of Organic Solids, Institute of Chemistry, Chinese Academy of Sciences, Beijing, China. <sup>2</sup>School of Chemical Sciences, University of Chinese Academy of Sciences, Beijing, China. <sup>3</sup>Laboratory for Chemistry of Novel Materials, Université de Mons, Mons, Belgium. ✉e-mail: [fjiaozhang@ucas.ac.cn](mailto:fjiaozhang@ucas.ac.cn); [dicha@iccas.ac.cn](mailto:dicha@iccas.ac.cn)

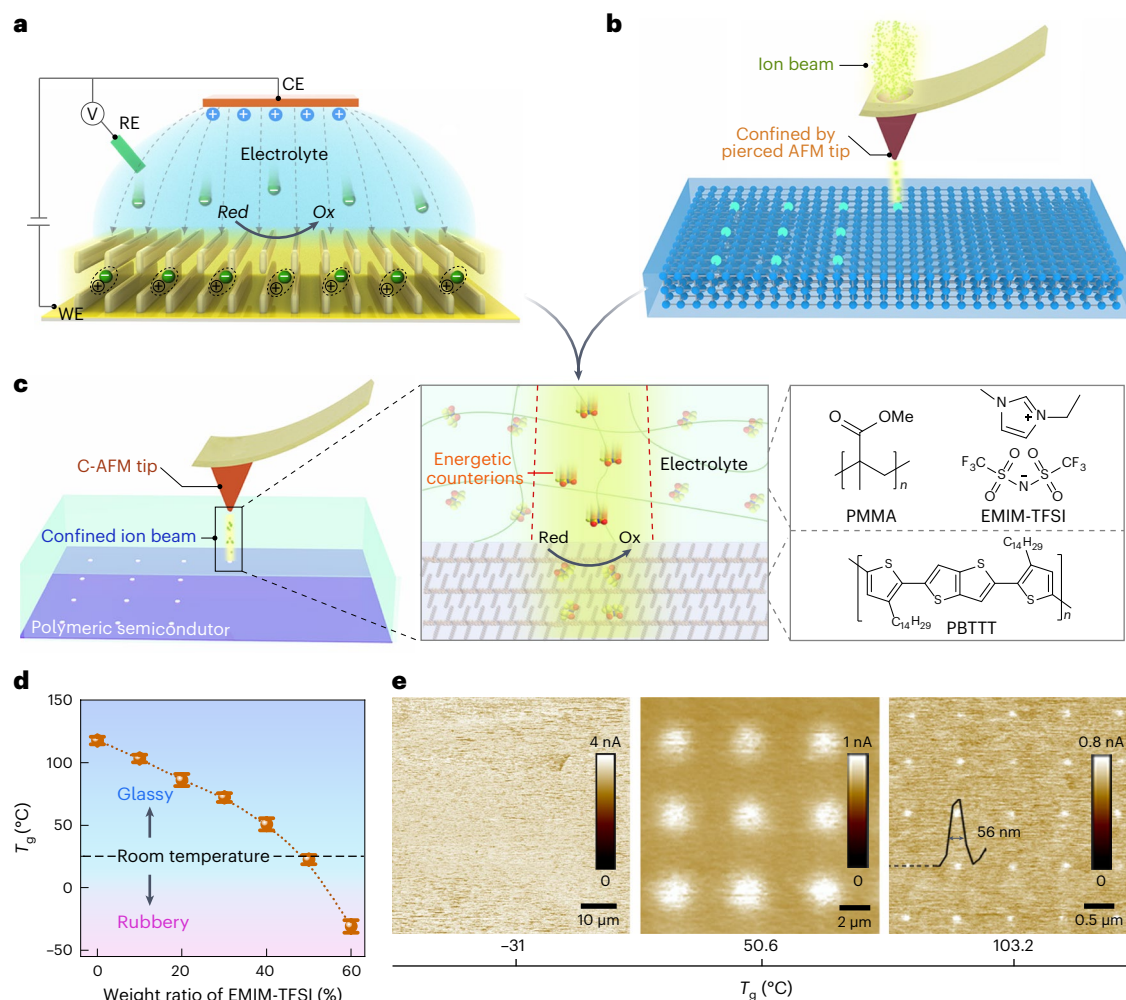


**Fig. 1 | Concept of NEII doping of polymeric semiconductors.** **a**, Schematic diagram of electrochemical doping for polymers, indicating that the redox process involves counterion penetration into polymers from the electrolyte but suffers from a fringing electric field. The electric field is in the opposite direction to the arrow. WE, working electrode; RE, reference electrode; CE, counterelectrode; Red, reduction; Ox, oxidation. **b**, Schematic diagram of single-ion implantation for inorganic electronics, where the ion beam is confined by a pierced AFM tip and is implanted into the target semiconductor. **c**, Diagram

showing the concept of NEII doping. The migration of counterions is confined by both the conductive AFM (C-AFM) tip and the reshaped fringing field in the electrolyte. Right: chemical structures of the electrolyte (PMMA and EMIM-TFSI) and the PBTTT polymeric semiconductor. **d**, The glass transition temperature ( $T_g$ ) of the electrolyte as a function of the weight ratio of EMIM-TFSI. Data are presented as mean  $\pm$  s.e. from uncertainties in fitting of the DSC curves with three values. **e**, Conductive AFM images of doped PBTTT films with different electrolyte  $T_g$ s. Inset: profile of the point with a doping resolution of 56 nm.

backbone and soft chains suffer irrecoverable damage, including cross-linking, scissions and graphitization, upon high ion bombardment<sup>6–8</sup>. It therefore remains of great interest to realize nanoresolved doping of polymeric semiconductors, ideally with a resolution down to <10 nm, to achieve the long-sought single-molecule-level doping.

Attempts have been made to address the resolution issue in polymers by combining chemical doping with confined photodoping or the photothermal effect<sup>3,9–11</sup>. However, the photophysical processes involved are bottlenecked by the diffraction limit, yielding a low doping resolution ranging from 200 nm to 5  $\mu$ m. Electrochemical doping offers a highly controllable approach for polymers, with precise manipulation of the electric field making it possible to accurately define the doping level<sup>12–14</sup>. Nevertheless, the inherent global charge compensation by counterions in the electrolyte produces a poor spatial resolution of  $10^2$ – $10^4$   $\mu$ m (refs. 15–18). It is worth noting that the migration of counterions to the host polymer in electrochemical doping can be considered analogous to ion implantation, but with ultralow-energy counterion species (Supplementary Note 1, Supplementary Fig. 1 and Supplementary Table 1). Under this hypothesis, nanoresolved doping

can be realized by creating a ‘nanostencil’ in the electrolyte to confine counterion migration. Unfortunately, the incompatibility of conventional nanolithography and polymeric films makes the nanostencil concept inapplicable to high-resolution electrochemical doping.

Here we present a concept, namely, nanoconfined electrochemical ion implantation (NEII) doping, that allows for precise doping of polymer by localizing the driving field for counterion migration in the electrolyte. By incorporating glassy insulating polymers with frozen segmental relaxation, lateral ion migration was suppressed in the polymer electrolyte, resulting in a highly localized electric field and anisotropic ion electromigration. We not only demonstrate a doping resolution of 56 nm with a carrier concentration over  $10^{19}$   $\text{cm}^{-3}$ , which is comparable to many inorganic counterparts, but more importantly, show a lowest lateral-extended doping length (LDL) of 9.3 nm, which is close to the polaron delocalization length of poly(2,5-bis(3-tetradecylthiophen-2-yl)thieno[3,2-*b*]thiophene) (PBTTT) polymers. Guided by the observation of a  $T_g - T$  dependent doping resolution for different materials (where  $T_g$  is the glass transition temperature and  $T$  is the operating temperature), high-performance polymer

devices with on-demand doping are demonstrated. Furthermore, the stamp-based NEII doping was demonstrated by employing a matrix tip array ( $2 \times 2 \text{ cm}^2$ ), offering an intriguing avenue for scalable nanoelectronics based on polymers.

## Design concept

The low spatial resolution of conventional electrochemical doping for polymeric semiconductors arises from the global electromigration of counterions, which is limited by the large size of the counterelectrode (CE) and the severe fringing field (Fig. 1a). Inspired by single-ion implantation in which ion beams are physically confined by a pierced AFM tip (Fig. 1b), we hypothesize that similar focused counterion beams can be achieved by creating intangible nanostencil via scaling the CE to the nanoscale and simultaneously linearly sharpening the fringing field (Fig. 1c). Accordingly, the ions from the electrolyte can migrate to the target semiconductor along the concentrated field lines, producing highly defined NEII doping. Following this concept, we utilize a nanosized AFM tip as the CE, and reshape the fringing field by manipulating the  $T_g$  of the electrolyte, as the fringing effect in electrochemical doping is highly associated with the glass-transition-related ion dynamics.

## $T_g$ -dependent doping resolution

To test the concept, we fabricated a series of polymer electrolytes with different  $T_g$  values by blending polymethylmethacrylate (PMMA) and 1-ethyl-3-methylimidazolium bis(trifluoromethylsulfonyl) imide (EMIM-TFSI) ionic liquid and explored the doping resolution based on a PBTTT film (Fig. 1c). Figure 1d presents the dependence of the electrolyte  $T_g$  on the weight ratio ( $W_{IL}$ ) of EMIM-TFSI. Due to the inherently high  $T_g$  of the PMMA insulators and the plasticizing effect of the ionic liquid, the resulting electrolytes exhibited a wide range of  $T_g$ s from 117.6 to  $-31 \text{ }^\circ\text{C}$  when the  $W_{IL}$  was increased from 0% to 60% (Extended Data Fig. 1). Specifically, these electrolytes exhibited distinguishable glassy and rubbery states at room temperature with a crossover point at 50%  $W_{IL}$ , whereas the electrolytes in both of these states exhibited smooth surfaces and uniform ion distributions (Supplementary Fig. 2). The two states with different  $T_g$  values allow precise modulation of ionic migration in the electrolyte, which could affect the field distribution and the doping resolution.

Figure 1e shows the current mapping of the doped PBTTT films produced by different electrolytes with various  $T_g$ s at room temperature. Interestingly, increasing the electrolyte  $T_g$  from  $-31$  to  $103.2 \text{ }^\circ\text{C}$  substantially enhanced the doping resolution, and the TFSI<sup>-</sup> anions implanted into entire films (100 nm) regardless of the  $T_g$  values (Extended Data Fig. 2 and Supplementary Figs. 3–6). When the electrolyte was rubbery with a  $T_g$  of  $-31 \text{ }^\circ\text{C}$ , the doped film exhibited a low doping spatial resolution of hundreds of micrometres (Supplementary Fig. 7), verifying that only using an AFM tip does not come close to achieving nanoscale doping. Once the electrolyte transitioned into a glassy state, an orders-of-magnitude improvement in the doping resolution could be observed. For instance, a micrometre-scale doping spatial resolution of  $\sim 2 \text{ }\mu\text{m}$  with uniform distribution was achieved with a  $T_g$  of  $50.6 \text{ }^\circ\text{C}$  (Supplementary Fig. 8). Further elevating the electrolyte  $T_g$  to  $103.2 \text{ }^\circ\text{C}$  resulted in a  $<100 \text{ nm}$  doping resolution with good stability in air (Supplementary Fig. 9). In particular, we achieved an outstanding resolution of 56 nm (average, 81 nm from 25 doping sites), which is several orders of magnitude higher than that of conventional electrochemical doping. The prominent resolution demonstrated the unique advantage of our proposed concept in realizing nanoscale doping of polymeric semiconductors.

The observed doping resolution ( $R_d$ ) is apparent rather than intrinsic because  $R_d$  is determined by both the CE–electrolyte contact size ( $L_c$ ) and the extended doping length (Fig. 2a). To reveal the intrinsic resolution, we define the LDL as  $(R_d - L_c)/2$  to evaluate the doping confinement. Taking into account the hollows that formed on the electrolyte surface due to the AFM tip, the  $L_c$  values was estimated to

be  $37.5 \pm 1.5 \text{ nm}$  (Fig. 2b and Extended Data Fig. 3), enabling the determination of the LDL values. As shown in Fig. 2c,  $R_d$  and LDL showed the same dependence on the electrolyte  $T_g$  for the low  $T_g$  region. However, a substantial LDL deviation was observed when  $T_g$  exceeded  $86 \text{ }^\circ\text{C}$ , indicating that a negligible effect of  $L_c$  on  $R_d$  could no longer be assumed. Of particular note, the aforementioned 56 nm resolution yielded the lowest LDL of 9.3 nm. Because the NEII doping is measured by conductive AFM, the determined LDL encompasses not only the ion-implantation-defined region but also the polaron delocalization extended doping. We therefore further performed theoretical simulation for the polaron delocalization length ( $L_{\text{polaron}}$ ) in both doped PBTTT oligomers and a  $3 \times 3 \pi$ -stacked tetramer-packed PBTTT matrix (Fig. 2d and Supplementary Fig. 10). Given that polarons can delocalize over 2–3 repeated units with a length of 2.6–3.8 nm, the minimal characterized LDL (9.3 nm) approached the detectable doping of PBTTT polymers. With this clear evidence, we expect that a  $<10 \text{ nm}$  apparent doping resolution is expected to be achievable once  $L_c$  can be scaled down to a few nanometres.

## Mechanism of nanoscale doping

Having identified the essential role of the electrolyte  $T_g$  in achieving nanoscale doping, we assessed the ion-migration-related dynamics of electrolytes. The electrolyte  $T_g$ -dependent ionic conductivity ( $\sigma_{\text{ion}}$ ) was determined by electrochemical impedance spectroscopy (EIS) (Supplementary Fig. 11). As expected, the ionic conductivity was exponentially suppressed by seven orders of magnitude, from  $7 \times 10^{-5}$  to  $3 \times 10^{-12} \text{ S}\cdot\text{cm}^{-1}$ , as the electrolyte  $T_g$  increased from  $-31$  to  $103.2 \text{ }^\circ\text{C}$  (Fig. 3a). Meanwhile, the doping resolution showed a proportional dependence on  $\sigma_{\text{ion}}$  in a log–log plot (Fig. 3b), demonstrating that the relatively low ionic conductivity in the high- $T_g$  electrolyte was responsible for the enhanced doping resolution. This deduction was further verified by observation of similar results for poly(vinylidene fluoride-co-hexafluoropropylene) (PVDF-HFP)- and poly(ethylene oxide) (PEO)-based electrolytes (Fig. 3a and Supplementary Fig. 12), with conductivities orders of magnitude higher than those for the PMMA/EMIM-TFSI electrolyte due to their much lower  $T_g$  (Extended Data Fig. 1).

In situ temperature-dependent EIS was performed to gain more insight into the ion-migration dynamics (Supplementary Fig. 13). The electrolyte with a  $T_g$  of  $51 \text{ }^\circ\text{C}$  was investigated because the glassy transition of such an electrolyte can be more readily modulated by elevated temperature. As shown in Fig. 3c, the ionic conductivity showed orders-of-magnitude enhancement with a crossover at  $51 \text{ }^\circ\text{C}$  when the temperature was increased from 0 to  $100 \text{ }^\circ\text{C}$ . Importantly, when the temperature was below  $T_g$ , the ionic conductivity can be described by the Arrhenius model, whereas the Vogel–Tammann–Fulcher (VTF) model better fits the ionic conductivity at elevated temperatures<sup>19</sup>. These two empirical forms can be expressed as  $\sigma_{\text{ion}} = \sigma_0 \exp\left(\frac{-E_a}{k_B T}\right)$  and  $\sigma_{\text{ion}} = A T^{-1/2} \exp\left(-\frac{E_b}{k_B(T-T_0)}\right)$ , respectively, where  $\sigma_0$  and  $A$  are the conductivity pre-exponential factors,  $E_a$  and  $E_b$  are the activation energies of ionic conduction,  $T_0$  is the thermodynamic glass transition temperature, which is usually 50 K lower than  $T_g$ , and  $k_B$  is the Boltzmann constant<sup>20</sup>. These two distinct ion-transport models revealed that decoupling and coupling of the ion dynamics occurred with segmental relaxation of the insulator matrix in the rubbery and glassy states of the electrolyte, respectively<sup>21</sup>. In the elevated temperature region where the electrolyte was in a rubbery state, the insulating segments underwent large-amplitude rearrangements (Supplementary Figs. 14 and 15), which reduced the energy barrier for ion migration from one coordination site to another<sup>22,23</sup>.

To quantitatively validate this assumption, we extracted the ionic activation energy for different  $T_g$  values under different operating temperatures (Supplementary Fig. 16). As shown in Fig. 3d, the measured activation energy  $E_b$  was sufficiently low, only tens of meV, which caused

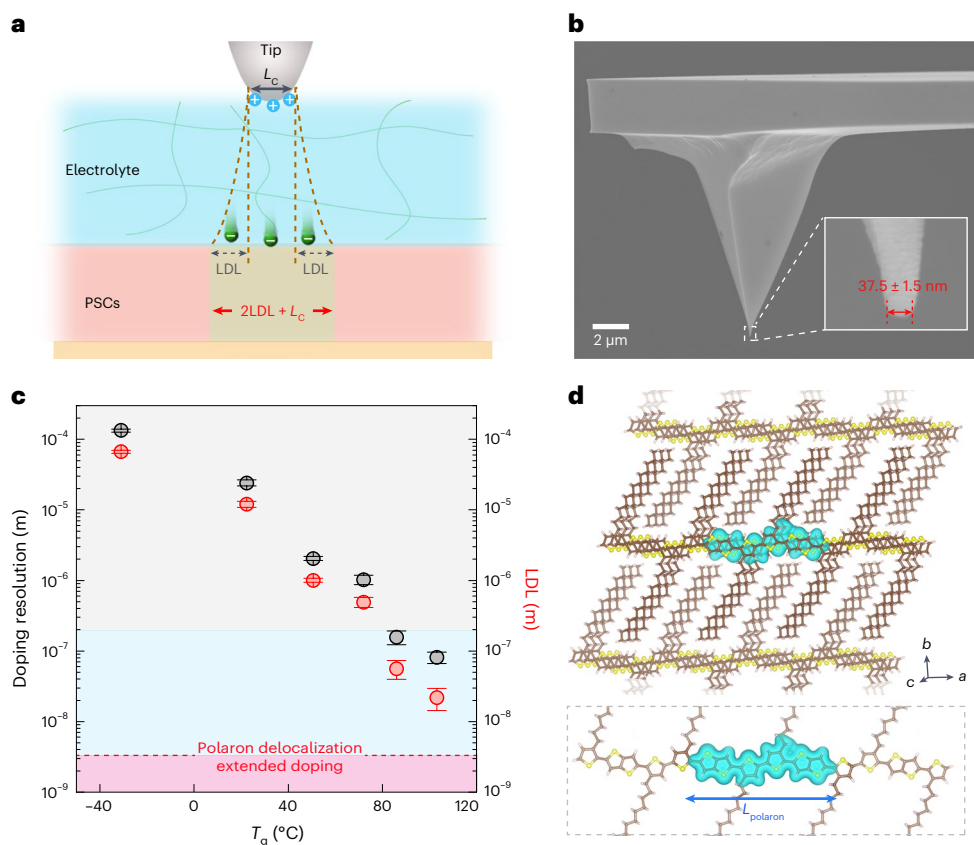


**Fig. 2 | Determination of the LDL of doped PBTTT film.** **a**, Schematic diagram showing how the apparent doping resolution is mainly determined by the LDL and the contact size ( $L_c$ ) between the tip and electrolyte. PSCs, polymeric semiconductors. **b**, SEM images of the SCM-PIT-V2 tip used in the experiment. Inset:  $L_c = 37.5 \pm 1.5$  nm, which is discussed in Supplementary Fig. 12. **c**,  $T_g$ -dependent doping resolution and LDL extracted from Supplementary Fig. 9.

The border between the light grey and blue regions is the doping resolution from existing reports, while the pink region represents the polaron delocalization extended doping of the polymers. Data are presented as mean  $\pm$  s.e. from three values of the doping sites, except for  $T_g = 103.2$  °C with up to 25 sites. **d**, Polaron delocalization length ( $L_{\text{polaron}}$ ) in the charged PBTTT with  $3 \times 3 \pi$ -stacked tetramer packing.

long-range ion dynamics and relatively high ionic conductivity in the electrolyte<sup>20</sup>. In contrast, when the electrolyte transformed into a glassy state, a much higher activation energy  $E_a$ , >450 meV, was extracted, which restricted ion migration in the electrolyte. It should be noted in particular that although this  $E_a$  value is high, it does not produce an obvious temperature change in the electrolyte in the optimized NEII doping condition (Supplementary Fig. 17). A further decrease in the ionic conductivity with decreasing temperature was attributed to a thermally activated ion-transport mechanism. The suppressed ion dynamics in the glassy state confirm our hypothesis that segmental relaxation of the insulating matrix is responsible for the increased activation energy.

With the aim of evaluating the effect of suppressed ion dynamics on the electrochemical doping resolution, we performed a finite-element simulation, as shown in Fig. 3e. The semiconductor was assumed to be a conducting electrode, and a negative point charge was used as the controlling electrode at a distance of 2,000 nm. The resulting field distributions at the semiconductor/electrolyte interface were compared to analyse the electrically driven ion migration behaviour (Supplementary Fig. 18). At a high ionic conductivity of  $10^{-3}$  S cm<sup>-1</sup>, a broad electric potential distribution near the semiconductor interface arose from the fringing effect, leading to macroscale doping of the semiconductors (Fig. 3e, lower left). In contrast, a more concentrated electric field could be observed at a lower  $\sigma_{\text{ion}}$  of  $10^{-7}$  S cm<sup>-1</sup> (Fig. 3e, lower middle). Specifically, when  $\sigma_{\text{ion}}$  was further decreased to  $10^{-8}$ – $10^{-13}$  S cm<sup>-1</sup>, the electric potential in the lateral direction was substantially eliminated, leading to a nearly vertical electric field beneath the probe that confines ion

migration. Combining experimental results and theoretical simulations (detailed discussion is provided in Supplementary Figs. 19–22), we conclude that the ion-migration capability originating from the polymer matrix with sluggish segmental relaxation is responsible for the linearly reshaped electric field, concentrated counterion migration, and thus the NEII doping. In other words, NEII doping should be universally achieved by manipulating the rubbery-glassy state transition of the electrolyte in electrochemical doping.

### Glass-transition-mediated nanoscale doping

Ionic migration in the electrolyte is not only associated with the electrolyte  $T_g$ , but also depends on the operating temperature ( $T$ )<sup>24</sup>, making the doping resolution probably sensitive to  $T_g - T$ . We thus measured the electrochemical doping resolution at various operating temperatures for different electrolyte  $T_g$ s. As shown in Fig. 4a, the doping resolution of all samples exhibited orders-of-magnitude enhancement with an exponential dependence as the temperature decreased from 100 to 0 °C, demonstrating the importance of tuning  $T$  relative to the electrolyte  $T_g$  to confine ion migration. Clearly, the doping resolution showed opposite dependences on  $T_g$  and  $T$ , and an inverse relation between the  $T_g - T$  was observed (Fig. 4b). In particular, this relation could be well fitted with an empirical equation of  $R_d = \exp(a(T_g - T) + b)$ , where  $a$  and  $b$  were determined to be  $-0.048$  and  $8.69$  in our case. We further demonstrated the generality of our approach in terms of material by applying it to three types of widely investigated high-mobility polymeric semiconductors, that is, thiophene-based poly(3-hexylthiophene-2,5-diyl) (P3HT), poly[[2,3,5,6-tetrahydro-2,

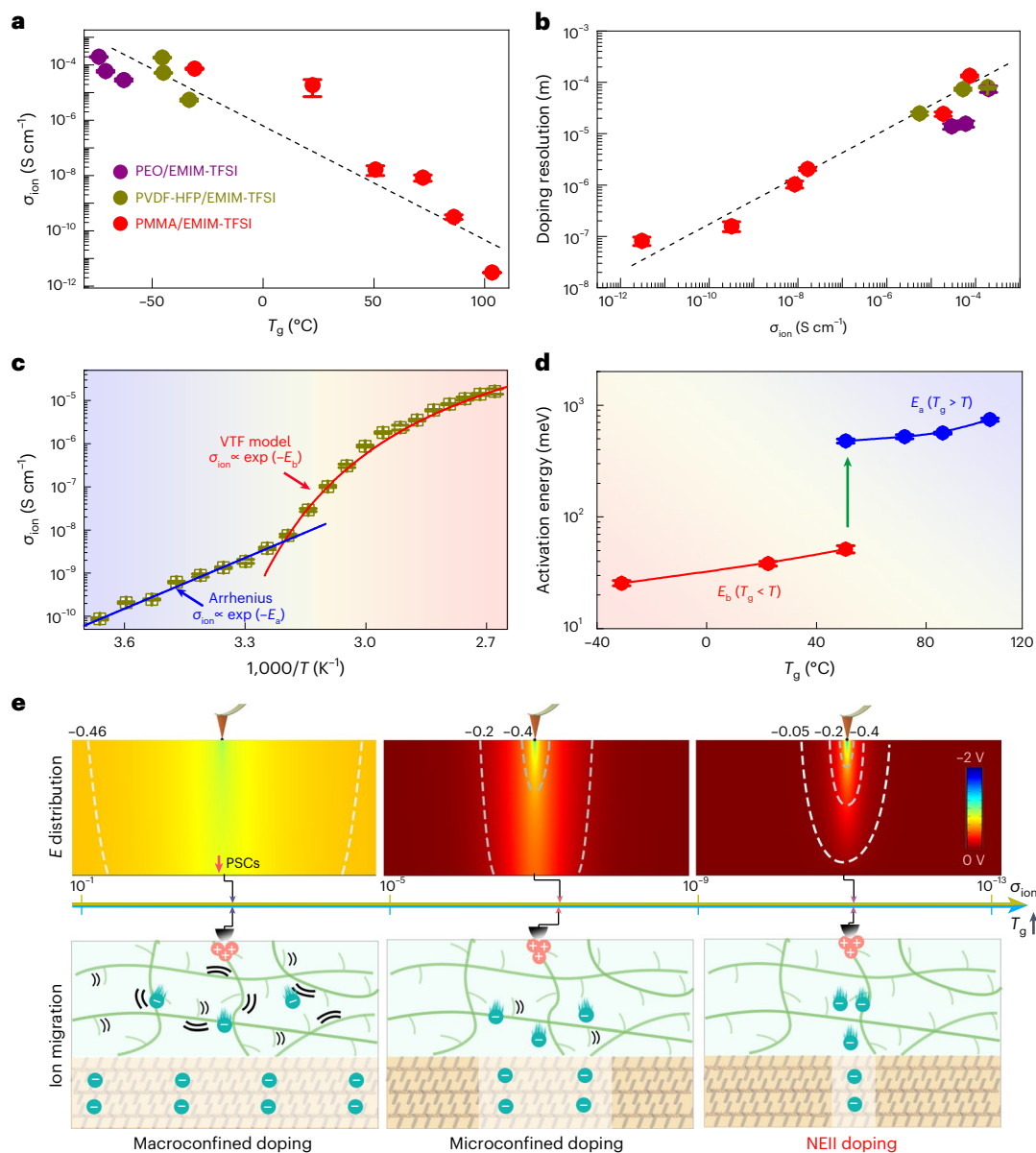


**Fig. 3 | Mechanism of  $T_g$ -dependent doping.** **a**,  $T_g$ -dependent ion conductivity for the PEO/EMIM-TFSI, PVDF-HFP/EMIM-TFSI and PMMA/EMIM-TFSI electrolytes with various weight ratios of EMIM-TFSI. Data are presented as mean  $\pm$  s.e. from uncertainties in fitting of the Nyquist plots with three values. **b**, Electrochemical doping resolution as a function of ionic conductivity. Data are presented as mean  $\pm$  s.e. of three values of the doping sites, except for  $T_g = 103.2$   $^{\circ}\text{C}$  with up to 25 sites. **c**, Temperature ( $1,000/T$ )-dependent ionic conductivity of the PMMA/EMIM-TFSI electrolyte with a 40% weight ratio of EMIM-TFSI. The blue and red curves are the fitted lines from the Arrhenius and the VTF model, respectively. Data are presented as mean  $\pm$  s.e. from uncertainties

in fitting of the Nyquist plots with three values. **d**, Activation energy as a function of electrolyte  $T_g$ .  $E_a$  and  $E_b$  are derived by using the Arrhenius and the VTF model, respectively. Data are presented as mean  $\pm$  s.e. from uncertainties in fitting of the temperature-dependent ionic conductivity curves with three values. **e**, Finite-element simulation of the electric field distribution. The bottom and top show diagrams of the ion migration dynamics in the rubbery and glassy states and the corresponding electric field distribution in the electrolytes, respectively. The scales in the x and y directions of the electric potential distribution are 100 and 2  $\mu\text{m}$ , respectively.

5-bis(2-octyldodecyl)-3,6-dioxopyrrolo[3,4-c]pyrrole-1,4-diyl]-2,5-thiophenediylthieno[3,2-b]thiophene-2,5-diyl-2,5-thiophenediyl (DPP-DTT) and indacenodithiophene-co-benzothiadiazole (IDTBT) polymers. Similar to the PBTTT film, the NEII doping for these materials can penetrate the entire film (Supplementary Figs. 23 and 24), and the resolution can be effectively controlled by manipulating electrolyte  $T_g - T$  (Fig. 4b). The highest doping resolutions optimized at  $T_g - T$  of 73.2  $^{\circ}\text{C}$  for P3HT, DPP-DTT and IDTBT were  $138 \pm 21.6$ ,  $141.3 \pm 4.9$  and  $82.3 \pm 4.5$  nm, respectively. The differences in doping resolutions are attributed to the varied ion-migration capabilities associated with

combined factors of side-chain structures, intermolecular packing of conjugated backbone, lamellar distance and overall crystallinity in film microstructures. Nevertheless, it is worth noting that all these doping resolutions represent benchmark values compared to previous doping results.

Our studies not only verify the achievement of nanoresolved doping, but also enable direct mapping of the  $T_g$ - and  $T$ -dependent doping resolution, as shown in Fig. 4c. Interestingly, we observe a nearly linear distribution of the doping resolution, which covers five orders of magnitude from millimetres to several tens of nanometres. Such a trend

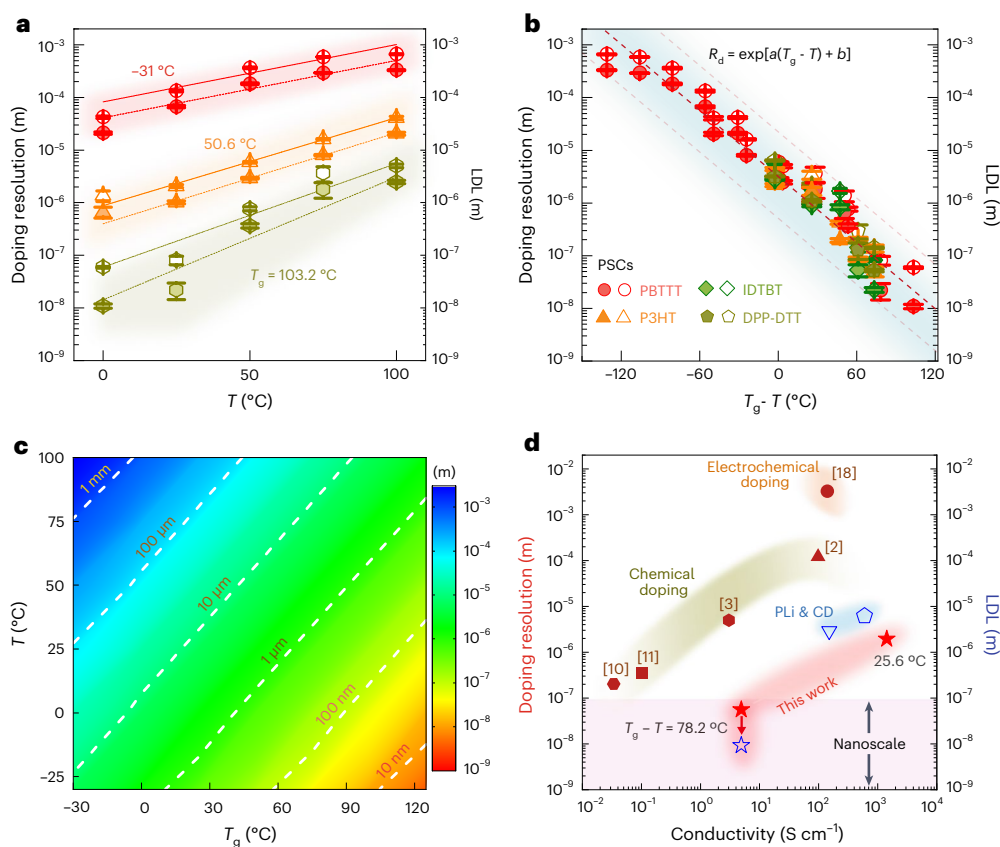


**Fig. 4** |  $T_g$ - and  $T$ -dependent doping resolution. **a**, Doping resolution as a function of  $T$ . The temperature-dependent doping resolution for different  $T_g$  shows a similar trend that can be well fitted by an exponential function. **b**,  $T_g - T$  dependent doping resolution summarized by the relation  $R_d = \exp[a(T_g - T) + b]$ . Data for **a, b** are presented as mean  $\pm$  s.e. of three values of the doping sites, except for  $T_g = 103.2^{\circ}\text{C}$  with up to 25 sites. **c**, Phase diagram showing the

evolution of doping resolution as a function of electrolyte  $T_g$  and operating temperature  $T$ . The colour bar shows the doping resolution. **d**, Comparison of the doping resolution (red solid scatters) and lateral-extended doping length (blue hollow scatters) with literature-reported conventional electrochemical doping, chemical doping, and photolithography and chemical doping (PLi & CD, Supplementary Fig. 26). The numbers in square brackets are reference numbers.

is consistent with the evolution of the ionic conductivity and segmental relaxation time of the polymer electrolyte. Looking beyond the NEII doping currently achieved, highly confined doping of other polymers can be expected by following the empirical relationship. For instance, submicroscale and  $<100$  nm doping resolution could in principle be obtained when  $T_g - T$  is  $>40^{\circ}\text{C}$  and  $>90^{\circ}\text{C}$ , respectively. Nevertheless, precise calibration should be further performed for a specific polymeric semiconductor because both the molecular structure and the aggregation structure affect the doping resolution. Even for the same polymers, films with an amorphous structure demonstrated a slightly superior doping resolution compared with their highly crystalline counterparts (Supplementary Fig. 25). More systematic investigations on NEII doping will allow rational doping design of polymeric semiconductors in accordance with the demands of diverse applications.

In comparison with other confined doping methods, such as chemical doping and conventional electrochemical doping, the key merit is the realization of a  $<100$  nm doping resolution with a  $<10$  nm LDL. Both values are among the lowest yet reported for polymer films, and are nearly thousands of times lower than those achieved by the conventional electrochemical process<sup>15–17,25,26</sup> and even orders lower than those produced by photolithography-technology-assisted chemical redox (Fig. 4d and Supplementary Figs. 26 and 27). A core task of semiconductor doping is to transform the host from a low-conductivity state to a high-conductivity state by introducing desired amounts of carriers. Although efficient doping can be easily obtained in macroscale doped films, achieving a high doping density at nanoscale resolution

has proven challenging. We demonstrated a doping density of  $10^{19} \text{ cm}^{-3}$  and a maximum conductivity of  $4.9 \text{ S cm}^{-1}$  (average,  $3.1 \text{ S cm}^{-1}$  from five devices, Supplementary Figs. 28–30) which were achieved even at nanoscale resolution. Notably, these electrical performances are among the best of those achieved by the conventional ion-implantation technique for silicon at the same doping resolution (Supplementary Fig. 31)<sup>27,28</sup>. The results illustrate that the NEII doping holds the potential to accelerate the advent of polymer nanoelectronics.

## NEII-doped devices

This study shows that NEII doping can be achieved by simply manipulating the electrolyte glass transition. Although similar to conventional ion implantation, this nanoscale doping has a number of benefits. For instance, it is non-destructive for weakly interacting polymers; it offers high controllability of the doping profile; almost infinite synthetically accessible salt ions can be incorporated; and the doping is very clean without any neutral or ion contamination. Together, these features make on-demand NEII doping highly valuable for polymer devices. For example, when a doping array was introduced into an organic thin-film transistor, a 200% enhancement in the field-effect mobility with negligible on/off ratio loss was observed (Fig. 5a,b and Supplementary Fig. 32). This enhancement can be attributed to the deterministic and discrete doping sites<sup>5</sup>. More interestingly, by performing both p- and n-type doping on an ambipolar PNDI2TEG-2Tz/PBTBT blended film (Fig. 5a and Supplementary Fig. 33), a seamless lateral p–n junction of 89 nm was realized with a rectification ratio of up to 5.7 (Fig. 5c and

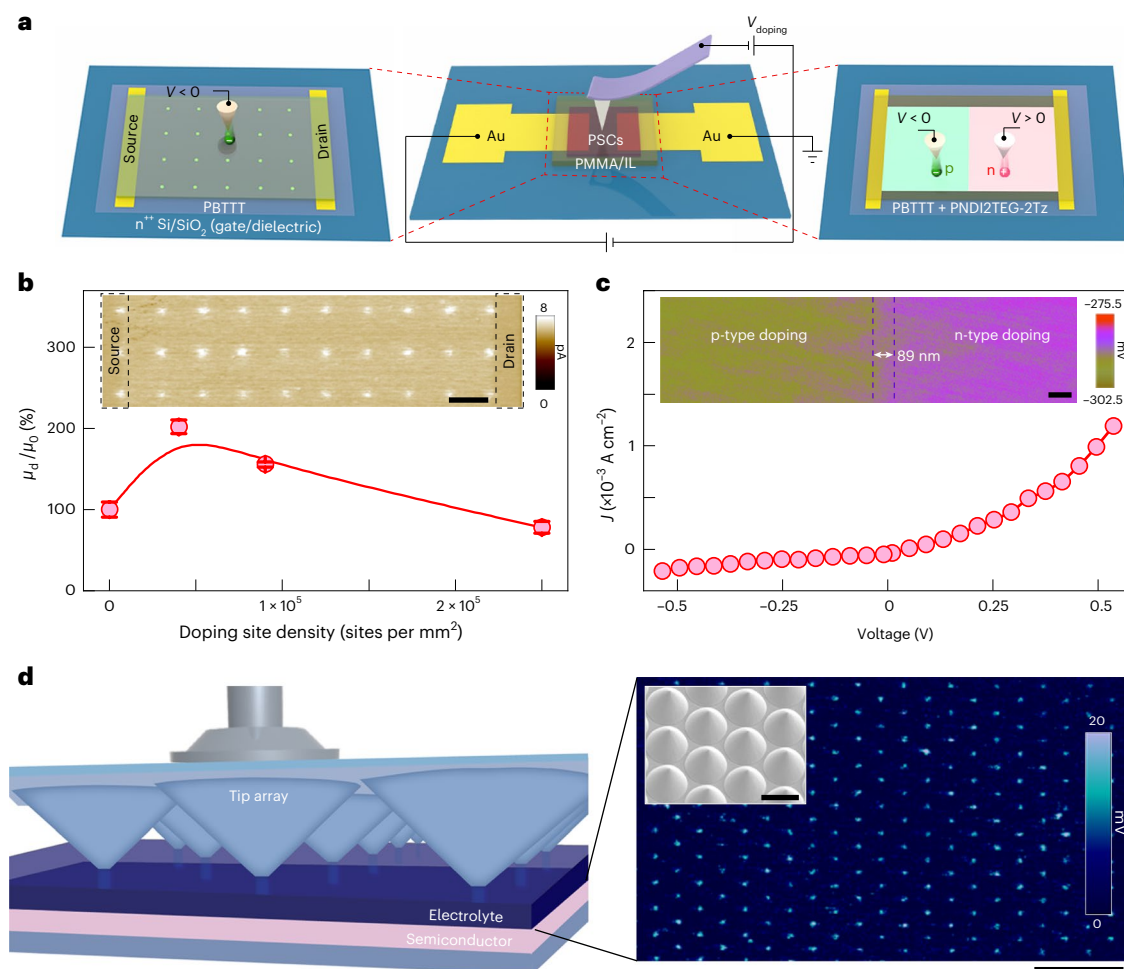


**Fig. 5 | NEII-doped devices.** **a**, Schematic diagram showing a transistor based on patterned doping films and a seamless lateral p–n junction. **b**, The mobility enhancement ( $\mu_d/\mu_0$ ) of the transistor as a function of doping density.  $\mu_d$  and  $\mu_0$  are the field-effect mobility for doped and pristine PBT TT films, respectively. Inset: representative conductive AFM image of the doped PBT TT transistors. Data are presented as the mean  $\pm$  s.e. from uncertainties in fitting of the transfer

curves with three values in Supplementary Fig. 32. Scale bar (inset), 2  $\mu$ m. **c**, Current density ( $J$ )–voltage characteristics of the p–n junction. Inset: Kelvin probe force microscopy image of the lateral p–n junction. Scale bar (inset), 200 nm. **d**, Demonstration of scalable NEII doping by using a tip array. Left: schematic diagram; right: Kelvin probe force microscopy image of the scalable NEII doping (scale bar, 10  $\mu$ m). Inset: SEM image of tip array (scale bar, 2.5  $\mu$ m).

Supplementary Fig. 34) and good stability (see Supplementary Figs. 9 and 35 for a detailed discussion). These achievements rival conventional high-resolution routes developed for inorganic counterparts<sup>29,30</sup>.

The applicability of our emerging NEII-doping method is bottlenecked by the complexity and slowness of the tip technique. To address this issue, we demonstrate the scaling capability of stamp-based NEII doping with an imprinting matrix tip. By applying a voltage and pressure to the tip array, we were able to achieve doping arrays of  $2 \times 2$  cm<sup>2</sup> in 10 s (Fig. 5d). This unique approach resulted in a uniform resolution of  $520 \pm 20$  nm, with a reproducible LDL<sub>avg</sub> of 82.5 nm. We noted that the present resolution is mainly limited by the large  $L_c$  ( $355.4 \pm 12.2$  nm) induced by the large commercial tip array used (Supplementary Fig. 36). Further improvement of the scalable resolution is expected if smaller tip radii become available. These unique features, combined with the benchmarking devices, emphasize the distinct advantages of our NEII-doping technique in unlocking the potential of polymers for soft nanoelectronics.

## Conclusion

We report a general way to achieve nanoscale doping in polymers by utilizing the NEII-doping concept. By adjusting the electrolyte  $T_g$  and  $T$ , we were able to create a linearly reshaped electric field distribution,

which facilitates nanoscale-confined counterion electromigration in the electrolyte. This produces a doping resolution of 56 nm for PBT TT films, with an LDL of 9.3 nm, which is close to the length of polaron delocalization extended doping. Our research empirically suggests that the doping resolution is strongly correlated with the  $T_g - T$  value of the electrolyte, providing a practical means for controlling nanoscale doping. More importantly, this approach is analogous to ion implantation in silicon electronics, and should be universally applicable to various materials for state-of-the-art polymer electronics. It should be noted that the current NEII-doping levels are still insufficient for many highly conductive applications. However, this limitation can largely be addressed by precisely tuning the physicochemical properties of dopant ions. Our findings, together with further achievements in doping-level manipulation, offer promise that the NEII-doping concept can serve as a powerful tool for exploring nanoscale polymeric optoelectronics.

## Online content

Any methods, additional references, Nature Portfolio reporting summaries, source data, extended data, supplementary information, acknowledgements, peer review information; details of author contributions and competing interests; and statements of data and code availability are available at <https://doi.org/10.1038/s41565-024-01653-x>.

## References

- Zheng, Y. Q. et al. Monolithic optical microlithography of high-density elastic circuits. *Science* **373**, 88–94 (2021).
- Kim, M. J. et al. Completely foldable electronics based on homojunction polymer transistors and logics. *Sci. Adv.* **7**, eabg8169 (2021).
- Perevedentsev, A. & Campoy-Quiles, M. Rapid and high-resolution patterning of microstructure and composition in organic semiconductors using ‘molecular gates’. *Nat. Commun.* **11**, 3610 (2020).
- WICK, G. L. Ion implantation. *Science* **170**, 425–427 (1970).
- Shinada, T., Okamoto, S., Kobayashi, T. & Ohdomari, I. Enhancing semiconductor device performance using ordered dopant arrays. *Nature* **437**, 1128–1131 (2005).
- Sviridov, D. V. Chemical aspects of implantation of high-energy ions into polymeric materials. *Russ. Chem. Rev.* **71**, 315–327 (2002).
- Moliton, A., Lucas, B., Moreau, C., Friend, R. H. & François, B. Ion implantation in conjugated polymers: mechanisms for generation of charge carriers. *Philos. Mag. B* **69**, 1155–1171 (2006).
- Popok, V. Ion implantation of polymers: formation of nanoparticulate materials. *Rev. Adv. Mater. Sci.* **30**, 1–26 (2012).
- Jacobs, I. E. et al. Reversible optical control of conjugated polymer solubility with sub-micrometer resolution. *ACS Nano* **9**, 1905 (2015).
- Bedolla et al. Reversible doping and photo patterning of polymer nanowires. *Adv. Electron. Mater.* **6**, 2000469 (2020).
- Jacobs, I. E. et al. Direct-write optical patterning of P3HT films beyond the diffraction limit. *Adv. Mater.* **29**, 1603221 (2017).
- Berggren, M. & Malliaras, G. G. How conducting polymer electrodes operate. *Science* **364**, 233 (2019).
- Kawasaki, M. & Iwasa, Y. ‘Cut and stick’ ion gels. *Nature* **489**, 510–511 (2012).
- Rivnay, J. et al. Organic electrochemical transistors. *Nat. Rev. Mater.* **3**, 17086 (2018).
- Ishiguro, Y., Inagi, S. & Fuchigami, T. Site-controlled application of electric potential on a conducting polymer ‘canvas’. *J. Am. Chem. Soc.* **134**, 4034–4036 (2012).
- Borgwarth, K., Rieken, C., Ebling, D. G. & Heinze, J. Surface characterisation and modification by the scanning electrochemical microscope (SECM). *Phys. Chem.* **99**, 1421–1426 (1995).
- Bargigia, I., Savagian, L. R., Osterholm, A. M., Reynolds, J. R. & Silva, C. Charge-transfer intermediates in the electrochemical doping mechanism of conjugated polymers. *J. Am. Chem. Soc.* **143**, 294–308 (2021).
- Bischak, C. G., Flagg, L. Q. & Ginger, D. S. Ion exchange gels allow organic electrochemical transistor operation with hydrophobic polymers in aqueous solution. *Adv. Mater.* **32**, e2002610 (2020).
- Vyazovkin, S. & Dranca, I. Physical stability and relaxation of amorphous indomethacin. *J. Phys. Chem. B* **109**, 18637–18644 (2005).
- Aziz, S. B., Woo, T. J., Kadir, M. F. Z. & Ahmed, H. M. A conceptual review on polymer electrolytes and ion transport models. *J. Sci. Adv. Mater. Dev.* **3**, 1–17 (2018).
- Zhao, Q., Stalin, S., Zhao, C.-Z. & Archer, L. A. Designing solid-state electrolytes for safe, energy-dense batteries. *Nat. Rev. Mater.* **5**, 229–252 (2020).
- Bresser, D., Lyonard, S., Iojoiu, C., Picard, L. & Passerini, S. Decoupling segmental relaxation and ionic conductivity for lithium-ion polymer electrolytes. *Mol. Syst. Des. Eng.* **4**, 779–792 (2019).
- Wang, Y. et al. Decoupling of ionic transport from segmental relaxation in polymer electrolytes. *Phys. Rev. Lett.* **108**, 088303 (2012).
- Ratner, M. A. & Shriver, D. F. Ion transport in solvent-free polymers. *Chem. Rev.* **88**, 109–124 (1988).
- Andersson Ersman, P. et al. All-printed large-scale integrated circuits based on organic electrochemical transistors. *Nat. Commun.* **10**, 5053 (2019).
- Tanaka, H. et al. Thermoelectric properties of a semicrystalline polymer doped beyond the insulator-to-metal transition by electrolyte gating. *Sci. Adv.* **6**, eaay8065 (2020).
- Zeiner, C. et al. Atypical self-activation of Ga dopant for Ge nanowire devices. *Nano Lett.* **11**, 3108–3112 (2011).
- Kanungo, P. D. et al. Ex situ n and p doping of vertical epitaxial short silicon nanowires by ion implantation. *Nanotechnology* **20**, 165706 (2009).
- Wang, G. et al. Seamless lateral graphene p–n junctions formed by selective in situ doping for high-performance photodetectors. *Nat. Commun.* **9**, 5168 (2018).
- Utama, M. I. B. et al. A dielectric-defined lateral heterojunction in a monolayer semiconductor. *Nat. Electron.* **2**, 60–65 (2019).

**Publisher’s note** Springer Nature remains neutral with regard to jurisdictional claims in published maps and institutional affiliations.

Springer Nature or its licensor (e.g. a society or other partner) holds exclusive rights to this article under a publishing agreement with the author(s) or other rightsholder(s); author self-archiving of the accepted manuscript version of this article is solely governed by the terms of such publishing agreement and applicable law.

© The Author(s), under exclusive licence to Springer Nature Limited 2024

## Methods

### Materials

PBTTT was synthesized and provided by I. McCulloch's group. Other semiconducting polymers, namely DPP-DTT, P3HT and IDTBT, were purchased from Sigma Aldrich. The PNDI2TEG-2Tz polymer was synthesized following a previous report<sup>31</sup>. The ionic liquid EMIM-TFSI (purity,  $\geq 99\%$ ; water content,  $\leq 500$  ppm) and PMMA insulators with an average  $M_w$  of  $\sim 120,000$  were purchased from Sigma Aldrich. PVDF-HFP and PEO were purchased from 3M and Alfa Aesar, respectively. All these materials were used as received without any purification.

### Device fabrication

Glass or n-doped silicon wafers with a 300 nm SiO<sub>2</sub> surface layer were used as substrates, and were cleaned with deionized water, alcohol and acetone, successively. Ti/Au (5/20 nm) electrodes were patterned by a shadow mask and thermally deposited on the substrates at a pressure of  $1 \times 10^{-6}$  mbar. Then, the semiconducting polymers were spin-coated onto the cleaned substrate at 3,000 r.p.m. for 60 s. All films were annealed at 200 °C for 2 h in a nitrogen glovebox and slowly cooled to room temperature, except for the PBTTT films which were annealed at 180 °C. For PBTTT polymers, the solvent was 1,2-dichlorobenzene, whereas DPP-DTT, P3HT and IDTBT were dissolved in chloroform. Specially, PBTTT in 1,2-dichlorobenzene solvent needed to be heated at 90 °C to improve the solubility. The thickness of all semiconducting films was around 50 nm, and was primarily controlled by varying the solution concentrations. Thereafter, the polymer electrolytes were fabricated by an 'on-the-fly dispensing spin-coating process'. Note that all electrolytes were fabricated by mixing ionic liquid and polymer insulators in n-butyl acetate (50 mg ml<sup>-1</sup>) with different weight ratios of EMIM-TFSI and stirred at 50 °C in a glovebox for at least 6 h.

### Electrochemical doping procedure and characterization

Electrochemical doping was performed in a Bruker Fastscan AFM instrument using a Peak Force Tuna module. Voltage pulses were applied through a Bruker SCM-PIT-V2 probe with platinum-iridium coatings (tip radius,  $\sim 25$  nm), whereas the evaporated Ti/Au electrodes were electrically connected to the sample stage. The doping position, doping voltage and duration was precisely controlled in a point-and-shoot fashion. For the temperature-dependent electrochemical doping, the devices were placed in a nitrogen environment and the temperature was controlled using a thermal application controller (Bruker). After performing the electrochemical doping, the electrolyte was immediately stripped off from the PBTTT films to enable non-volatile electrochemical doping (as discussed in Supplementary Fig. 3), and to expose the doped film for ease of characterization of its composition, electronic structure and doping resolution (Supplementary Figs. 4–7). The doping resolution was measured by either taking optical images or mapping current–voltage characteristics (Peak Force Tuna module in a Bruker Fastscan AFM instrument) at ambient temperature.

### Thermal transition measurements

The polymer electrolytes were prepared by blending the EMIM-TFSI ionic liquid and polymer insulators in a low-boiling-point acetone solvent, and then dried at 180 °C in a vacuum oven for 6 h. The  $T_g$  of the polymer electrolytes were measured by differential scanning calorimetry (DSC2-00881). A 5 mg sample was used and sealed in a hermetic aluminium pan to measure the dynamic scanning calorimetry thermograms. The sample was heated and cooled in two cycles between  $-76$  to 180 °C. The heating and cooling speeds for all these measurements were 10 °C min<sup>-1</sup>.

### Ultraviolet–visible spectroscopy to determine the $T_g$ of polymeric semiconductors

The as-cast semiconductor films were prepared on quartz glass and dried under vacuum for over 30 min. The films were heated at each

temperature for 10 min on a hot plate and then suspended in air and allowed to cool to room temperature. The absorption of as-cast and annealed films was recorded using a ultraviolet–visible–near-infrared spectrophotometer (Shimadzu UV-2600) at room temperature, and the baseline was collected with a blank substrate of quartz glass. To quantitatively determine the  $T_g$ , a deviation metric (DM<sub>T</sub>)<sup>32</sup> was defined as the sum of the squared deviation in the absorbance between as-cast and annealed films

$$DM_T = \sum_{\lambda_{\min}}^{\lambda_{\max}} [I_{RT}(\lambda) - I_T(\lambda)]^2$$

where  $\lambda_{\max}$  and  $\lambda_{\min}$  are the wavelengths of the lower and upper bounds of the optical sweep, and  $I_{RT}(\lambda)$  and  $I_T(\lambda)$  are the normalized absorption intensities for the as-cast and annealed films, respectively. The  $T_g$  values are finally determined by plotting DM<sub>T</sub> against annealing temperature.

### Time-of-flight secondary ion mass spectrometry characterization

Time-of-flight secondary ion mass spectrometry (M6, IONTOF) analysis with Bi<sub>3</sub><sup>+</sup> (30 keV) as the primary ion source was used to determine the doping profile; negative secondary ions from an area of  $50 \times 50 \mu\text{m}^2$  were detected. Sputter etching was performed over an area of  $400 \times 400 \mu\text{m}^2$  using an argon gas cluster ion beam with an acceleration voltage of 5 keV. The currents of the primary ion beam and the argon gas cluster ion beam were 1.0 pA and 1.0 nA, respectively, for all doped polymeric semiconductor films.

### Scanning electron microscopy energy-dispersive spectroscopy characterization

Samples were prepared by spin-coating the electrolyte solutions onto the cleaned n-doped silicon substrate. The thickness of all electrolytes was controlled at  $\sim 2 \mu\text{m}$ , by modulating both electrolyte concentration and coating speed. The scanning electron microscopy (SEM) analysis was performed on a Hitachi SU8020 at 5 kV and energy-dispersive spectroscopy (EDS) was acquired with an Oxford Ultim Extreme to study the spatial distribution of elemental sulfur, nitrogen and fluorine.

### Ultraviolet–visible–near-infrared spectroscopy

The samples for ultraviolet–visible–near-infrared measurement were prepared as follows: (1) PBTTT film and PMMA/EMIM-TFSI electrolyte were successively spin-coated on a quartz glass substrate and device fabrication was completed by evaporating 60 nm aluminium on top of the electrolyte; (2) electrochemical doping was performed by applying a voltage (0 to  $-4$  V) on the aluminium electrode for 100 s; (3) both the electrolyte and electrode were immediately stripped off from the semiconductor layer. All ultraviolet–visible–near-infrared spectra of the PBTTT thin films were recorded in air using a JASCO V-570 spectrometer.

### EIS measurements

The EIS measurements were based on the gold/electrolyte/aluminium capacitor. All spectra were determined from a.c. impedance measurements using an electrochemical workstation (CHI-760E, CH Instruments) in the frequency range starting from 1,000 kHz to lower values. For temperature-dependent EIS, the devices were cooled/heated in the range from 0 to 100 °C set by a temperature controller (TETF-LN). Prior to the measurements, thermal stabilization for 20 min was performed. The ionic conductivity,  $\sigma_{\text{ion}}$ , was calculated from the following equation:

$$\sigma_{\text{ion}} = \frac{t}{R_b A} \quad (1)$$

where  $t$  is the thickness of the sample,  $A$  is the capacitor area and  $R_b$  is the bulk resistance of the electrolyte.

### X-ray and ultraviolet photoelectron spectroscopy characterization

All samples for X-ray and ultraviolet photoelectron spectroscopy measurements were prepared in the same way as for ultraviolet–visible–near-infrared spectroscopy, and were characterized by using a Kratos AXIS ULTRA DLD photoelectron spectroscopy system in an ultrahigh vacuum. A monochromatic Al K $\alpha$  X-ray (1,486.6 eV) and a helium-discharge lamp (21.22 eV) were taken as the excitation sources, respectively. A bias voltage of  $-9$  V was applied to obtain the secondary-electron cut-off region. The Fermi edge was calibrated from a ultraviolet photoelectron spectrum of the Ar $^{1+}$ -sputtered clean gold substrate and is referred to as the zero binding energy in all spectra.

### Transfer coefficient measurement

The transfer coefficient ( $\alpha$ ) of the electrolyte-based capacitor was determined by measuring the polarization curves according to the Tafel method. All measurements were performed using an electrochemical workstation (CHI-760E, CH Instruments) at room temperature. The scanning rate of the measurement was  $0.01$  V s $^{-1}$  and the quiet time was 2 s in Tafel plot mode.

### Grazing-incidence wide-angle X-ray scattering characterization

Grazing-incidence wide-angle X-ray scattering measurements were conducted on an Anton Paar SAXSpot 5.0 system with an X-ray wavelength of 1.5418 Å and an incidence angle of  $0.1^\circ$ . The diffraction intensity was detected with a two-dimensional Hybrid Photon Counting detector (PILATUS3R1M). All X-ray measurements were performed in a vacuum environment to minimize air scattering and beam damage to samples.

### COMSOL finite-element simulation

For electrochemical modules with a tertiary current distribution, the Nernst–Planck interface in COMSOL Multiphysics was utilized to simulate the electric potential distribution and equipotential lines in the polymer electrolyte. A two-dimensional model of the electrochemical device was designed to perform this simulation and the boundary setting is shown in Supplementary Fig. 18. The model consists of a nano-electrode and a bottom electrode with widths of 10 nm and 100  $\mu$ m, respectively, and an electrolyte 2,000 nm thick sandwiched in between. The electrode reaction at the electrode–electrolyte interface boundary was expressed by the Butler–Volmer equation, wherein the cathodic transfer coefficient was defined as 0.5 and the reference exchange current density was determined by measuring the Tafel curve (Supplementary Fig. 22) based on a gold/electrolyte/aluminium capacitor structure. Considering ion accumulation in the electrode–electrolyte interface, a double-layer capacitance node was also added, and the capacitance of electrolytes with different  $T_g$  were characterized with an LCR meter (ECA 200). The electrolyte ionic conductivities were varied to compare the electric potential distribution (Fig. 3e), while the  $\sigma_{\text{ion}}$  values were determined from EIS measurements.

### Density functional theory calculations

The  $L_{\text{polaron}}$  calculations were carried out by density functional theory (DFT) with the VASP code, while the PBTTT stacking conformational optimization follows previous work<sup>33</sup>. The Perdew–Burke–Ernzerhof functional within the generalized gradient approximation was used to process the exchange correlation, while the projector augmented wave pseudopotential was applied with a kinetic energy cut-off of 500 eV, and was utilized to describe the expansion of the electronic eigenfunctions. The Brillouin-zone integration was sampled by a  $\Gamma$ -centred  $5 \times 5 \times 1$  Monkhorst–Pack  $k$ -point. All atomic positions were fully relaxed until energy and force reached a tolerance of  $1 \times 10^{-5}$  eV and  $0.03$  eV Å $^{-1}$ , respectively. The dispersion-corrected DFT-D method was used to consider the long-range interactions. The simulation of the

infrared spectra of doped PBTTT film was done at the DFT level using the B97XD functional and the 6-31G\*\* basis set using the Gaussian16, revision C.03 package<sup>34</sup>.

### Data availability

The relevant raw data for this study are available for research purposes from the corresponding authors upon reasonable request. Source data are provided with this paper.

### Code availability

The code that supports the theoretical plots within this paper is available from the corresponding authors upon reasonable request.

### References

1. Liu, J. et al. N-type organic thermoelectrics of donor–acceptor copolymers: improved power factor by molecular tailoring of the density of states. *Adv. Mater.* **30**, e1804290 (2018).
2. Ghasemi, M. et al. A molecular interaction–diffusion framework for predicting organic solar cell stability. *Nat. Mater.* **20**, 525–532 (2021).
3. Venkateshvaran, D. et al. Approaching disorder-free transport in high-mobility conjugated polymers. *Nature* **515**, 384–388 (2014).
4. Frisch, M. J. et al. Gaussian 16, revision C.01 (2016).

### Acknowledgements

The authors acknowledge financial support from the National Natural Science Foundation (22125504, 22021002, 22305253, U22A6002), the Strategic Priority Research Program of the Chinese Academy of Sciences (XDB0520000), the Beijing Municipal Natural Science Foundation (Z220025), the K. C. Wong Education Foundation (GJTD-2020-02), the China Postdoctoral Science Foundation (119103S395), Fundamental Research Funds for the Central Universities (E1E40301X2, E2E40305X2), CAS (ZDBS-LYSLH034). We thank W. Zhang and I. McCulloch (Imperial College London) for providing the PBTTT polymers. We appreciate J. Jiang (Institute of Chemistry, Chinese Academy of Sciences) for the valuable discussion on the mechanism part. The work in Mons has received funding from the European Union's Horizon 2020 research and innovation programme under grant agreement number 964677 (MITICS) and computational resources have been provided by the Consortium des Équipements de Calcul Intensif (CÉCI), funded by the Fonds de la Recherche Scientifique de Belgique (FRS-FNRS) under grant number 2.5020.11 and by the Walloon Region. D.B. is FNRS Research Director.

### Author contributions

C.D. and F.Z. conceived and led the research. D.Z. supervised the project. C.D., L.X., F.Z. and Z.H. proposed the concept and designed the experiments. L.X. did the device fabrication, measurements, analysed the data and performed the simulations. C.D. and L.X. wrote the main manuscript with comments from all authors. C.Y. measured the  $T_g$  of semiconductors and performed the grazing-incidence wide-angle X-ray scattering experiments. Y. Zhao performed the time-of-flight secondary ion mass spectrometry measurements. Z.L. performed the infrared temperature measurements. Y.M. commented on the organization of the manuscript. Z.J. helped with the lithography process for the electrode pattern. V.L. and D.B. performed the infrared simulation of the charged polymer. Q.M. and L.J. helped with electrochemical doping. L.L. helped with scanning electron microscopy/energy-dispersive spectroscopy measurements. X.D. performed X-ray and ultraviolet photoelectron spectroscopy measurements and DFT calculations. Y. Zou helped with the X-ray and ultraviolet photoelectron spectroscopy analysis. D.Z. guided the synthesis of PNDI2TEG-2Tz polymer and commented on the manuscript. All authors contributed to the preparation of the final draft.

**Competing interests**

The authors declare no competing interests.

**Additional information**

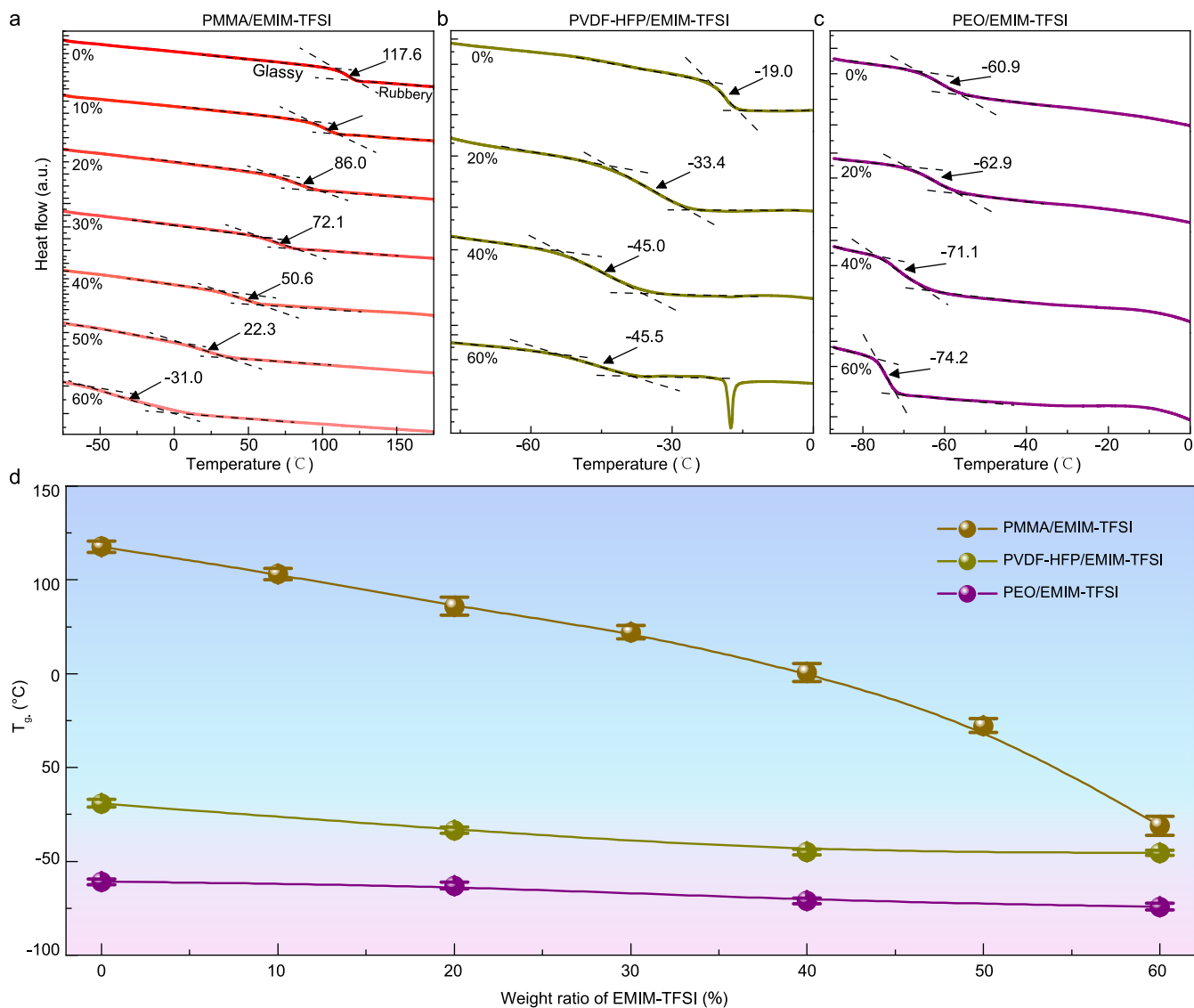
**Extended data** is available for this paper at <https://doi.org/10.1038/s41565-024-01653-x>.

**Supplementary information** The online version contains supplementary material available at <https://doi.org/10.1038/s41565-024-01653-x>.

**Correspondence and requests for materials** should be addressed to Fengjiao Zhang or Chong-an Di.

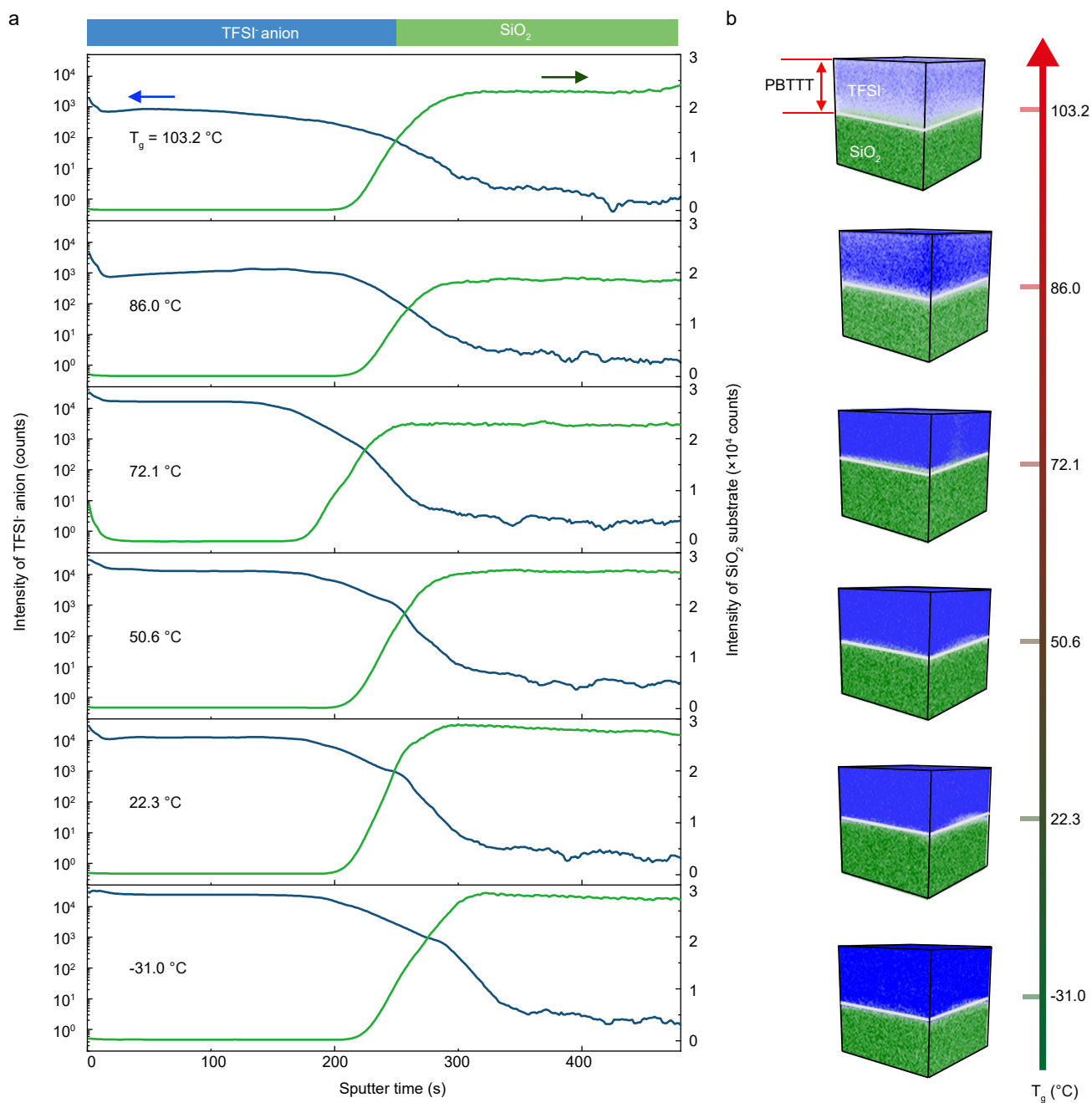
**Peer review information** *Nature Nanotechnology* thanks Ying Diao and the other, anonymous, reviewer(s) for their contribution to the peer review of this work.

**Reprints and permissions information** is available at [www.nature.com/reprints](http://www.nature.com/reprints).



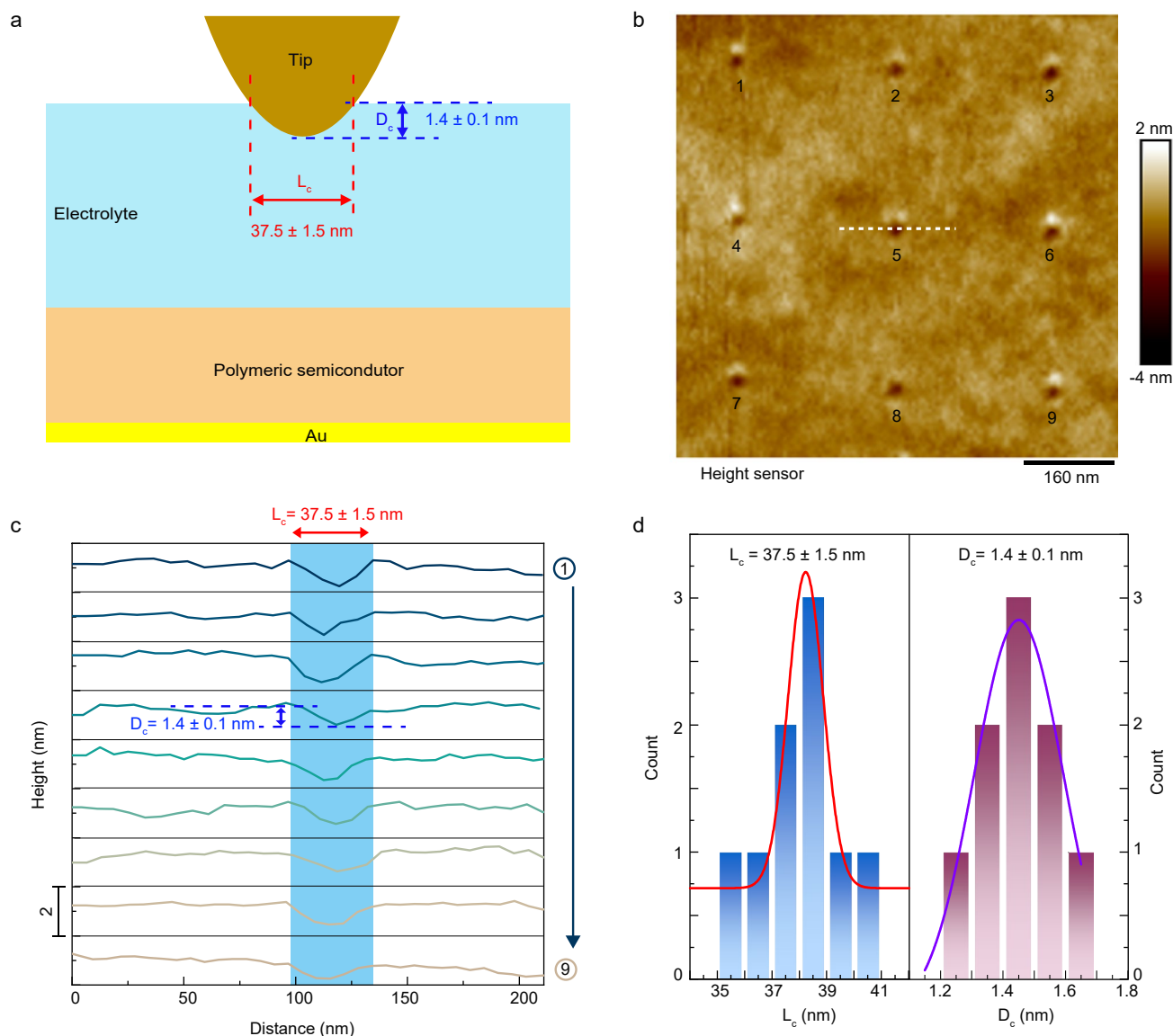
**Extended Data Fig. 1 | Determination of the electrolyte  $T_g$ .** a-c, Differential scanning calorimeter thermal analysis curves of (a), PMMA/EMIM-TFSI, (b), PVDF-HFP/EMIM-TFSI and (c), PEO/EMIM-TFSI electrolytes with different weight ratio of EMIM-TFSI ionic liquid. The determination of electrolyte  $T_g$  was shown in

the figure by extracting the midpoint between rubber and glass baselines. d, Comparison of the glass transition temperature these three electrolytes with varying weight ratio of EMIM-TFSI. Data are presented as mean  $\pm$  standard error from 3 uncertain values in fitting of the DSC curve.



**Extended Data Fig. 2 | Doping depth analysis of the films with different electrolyte  $T_g$  values.** **a**, TOF-SIMS profiles of the TFSI<sup>-</sup> and SiO<sub>2</sub> signals as a function of sputtering time. The thickness of the films was 100 nm and were doped under different electrolyte  $T_g$  values. **b**, 3D tomography images of TFSI<sup>-</sup> anion in the PBTTT film that constructed from the depth profiles of graph (a).

The blue and green points represent the distribution of TFSI<sup>-</sup> anion and SiO<sub>2</sub> substrate, respectively. It can be observed that the TFSI<sup>-</sup> dopant existed within the whole thickness of 100 nm for all electrolyte  $T_g$ , although the injected ion dose decreased at the high electrolyte  $T_g$ .



**Extended Data Fig. 3 | Determination of the contact size ( $L_c$ ) between AFM tip and electrolyte.** **a**, Schematic illustration of the contact between the AFM tip and electrolyte. Given the soft nature of the electrolyte, regular hollows on the electrolyte would be induced by the AFM tip that could be used to estimate the contact area between the tip and electrolyte. **b**, AFM height image of the

PMMA/EMIM-TFSI (10%) electrolyte surface after NEII doping. **c**, Height profiles of the hollow array, which are derived from 9 sites as depicted in graph (**b**). **d**, Statistical distribution histograms of  $L_c$  (left) and  $D_c$  (right). The  $D_c$  means the depth of the hollow. All data are presented as mean  $\pm$  standard error from 9 values that extracted from the hollows.